

Silica-induced Chronic Inflammation Promotes Lung Carcinogenesis in the Context of an Immunosuppressive Microenvironment^{1,2}

Javier Freire^{*,3}, Daniel Ajona^{*,3}, Gabriel de Biurrun^{*},
Jackeline Agorreeta^{*,†}, Victor Segura^{*},
Elizabeth Guruceaga^{*}, Anne-Marie Bleau^{*},
Ruben Pio^{*,‡}, David Blanco^{*,†} and Luis M. Montuenga^{*,†}

^{*}Center for Applied Medical Research (CIMA), Pamplona, Spain; [†]Department of Histology and Pathology, School of Medicine, University of Navarra, Pamplona, Spain; [‡]Department of Biochemistry and Genetics, School of Medicine, University of Navarra, Pamplona, Spain

Abstract

The association between inflammation and lung tumor development has been clearly demonstrated. However, little is known concerning the molecular events preceding the development of lung cancer. In this study, we characterize a chemically induced lung cancer mouse model in which lung cancer developed in the presence of silicotic chronic inflammation. Silica-induced lung inflammation increased the incidence and multiplicity of lung cancer in mice treated with *N*-nitrosodimethylamine, a carcinogen found in tobacco smoke. Histologic and molecular analysis revealed that concomitant chronic inflammation contributed to lung tumorigenesis through induction of preneoplastic changes in lung epithelial cells. In addition, silica-mediated inflammation generated an immunosuppressive microenvironment in which we observed increased expression of programmed cell death protein 1 (PD-1), transforming growth factor- β 1, monocyte chemotactic protein 1 (MCP-1), lymphocyte-activation gene 3 (LAG3), and forkhead box P3 (FOXP3), as well as the presence of regulatory T cells. Finally, the *K-RAS* mutational profile of the tumors changed from Q61R to G12D mutations in the inflammatory milieu. In summary, we describe some of the early molecular changes associated to lung carcinogenesis in a chronic inflammatory microenvironment and provide novel information concerning the mechanisms underlying the formation and the fate of preneoplastic lesions in the silicotic lung.

Neoplasia (2013) 15, 913–924

Introduction

Lung cancer is the leading cause of cancer-related mortality in the world, causing more deaths per year than the next two more deadly cancers combined [1]. A number of lung cancer etiological factors have been clearly identified: tobacco smoke, primarily, but also cooking oil vapor, burning coal, radon, air pollution, and occupational exposure to asbestos and other carcinogens [2]. Most of these insults also trigger pulmonary inflammation, which appears to exhibit dysregulation in parallel to the carcinogenic process [3,4]. Interestingly, several studies have shown that long-term consumption of anti-inflammatory drugs, such as aspirin and specific cyclooxygenase-2 inhibitors, are associated with a reduced incidence of lung cancer [5,6]. Failure to control the inflammatory response is associated with active recruitment of stromal and inflammatory cells that, in turn, change the tumor microenvironment. The continuous infiltration of these cells incites tissue reparative proliferation in cytokine- and growth factor-enriched stroma [7]. All of

these events may lead to sequential preneoplastic changes of the respiratory epithelium; some of these changes will eventually develop into lung carcinoma [8]. In fact, inflammation and carcinogenesis share common mechanistic hallmarks [9]. Importantly, chronic inflammation is also associated with the induction of immune-suppressive mechanisms, such

Abbreviations: NDMA, *N*-nitrosodimethylamine; Tregs, regulatory T cells
Address all correspondence to: Luis M. Montuenga, PhD, Division of Oncology, CIMA Building, Pio XII 55, 31008 Pamplona, Spain. E-mail: lmontuenga@unav.es

¹This work was supported by the UTE project CIMA and the Spanish Ministries of Health/Economy and Competitiveness (ISCIII: RTICC RD12/0036/0040, FIS-PI 04/2128, and 10/00166). No potential conflicts of interest declared.

²This article refers to supplementary materials, which are designated by Tables W1 to W3 and Figures W1 to W4 and are available online at www.neoplasia.com.

³These authors contributed equally to this work.

Received 23 January 2013; Revised 31 May 2013; Accepted 10 June 2013

Copyright © 2013 Neoplasia Press, Inc. All rights reserved 1522-8002/13/\$25.00
DOI 10.1593/neo.13310

as the accumulation of myeloid-derived suppressor cells and regulatory T cells (Tregs). These cell types inhibit antitumor immunity by blocking the activation of immune effector cells [10–12]. The blockade of the programmed cell death protein 1 (PD-1)/PD-L1 axis, which negatively regulates T cell responses, has recently been shown to provide clinical benefit in patients with advanced non-small cell lung cancer, with durable response in 6% to 18% of the treated cases [13,14].

The contribution of known oncogenes and tumor suppressor genes to lung carcinogenesis has been demonstrated in previous reports using genetically engineered mouse models [15]. However, additional animal models that analyze the effects of airway inflammatory conditions upon cellular and molecular events in lung carcinogenesis are needed [16]. In this study, we developed a chemically induced lung cancer model to study the role of chronic inflammation in lung carcinogenesis. For that purpose, we used a low tumorigenic dose of *N*-nitrosodimethylamine (NDMA) in combination with oropharyngeal administration of silica. Our model is unique in both the type of inflammatory condition we use to promote cancer and the sequential analysis of malignant lesions that allows us to study separately the effects of inflammation in preneoplastic and full neoplastic lesions.

Silicosis is an occupational health concern. About 3 million workers in Europe were exposed to crystalline silica from 1990 to 1993. Silica exposure has been associated with several disorders, among which airway obstruction (chronic obstructive pulmonary disease) and lung cancer are related to our model. Several meta-analysis generally demonstrate a significant increased risk of lung cancer in patients with silicosis [17]. In mice, silica induces a permanent inflammatory condition in lungs, and marked cellular and stromal changes occur within lung parenchyma; however, it does not lead to lung carcinogenesis [18]. In this study, we show that the inflammatory microenvironment induced by silica markedly increases the incidence and multiplicity of preneoplastic adenomatous lesions and lung adenocarcinoma in mice treated with NDMA. Our findings also indicated that inflammation promotes distinct mutational alterations and, interestingly, increases the number of Tregs in lung stroma. Microarray-based gene expression analysis revealed that, in the presence of silica, lung tumor cells markedly overexpress immunosuppressive genes.

Taken together, our study provides a useful new multistep animal model for examining the specific role of chronic inflammation in promoting lung carcinogenesis and identifies for the first time molecular mechanisms by which silica-mediated inflammation creates a favorable microenvironment for tumor progression.

Materials and Methods

Animal Model and Reagents

Eight-week-old female Balb/c mice were purchased from Harlan Laboratories (Indianapolis, IN). All mouse experiments were approved by the Ethics Committee on Animal Research of the University of Navarra.

Both NDMA (Sigma, St Louis, MO) and silica (US Silica Co, Berkeley Springs, WV) were resuspended in neutral-buffered saline and sonicated for 30 seconds. Mice were treated with oropharyngeal aspiration with a single dose of 7.5 mg/kg NDMA, 9 mg of silica, a combination of both, or saline in a final volume of 90 μ l, as previously described [19]. The NDMA dose was determined as the minimal amount of carcinogen able to induce lung tumorigenesis in mice without toxic side effects (data not shown). The amount of instilled

silica was chosen as a dose that triggers lung inflammation with minimal toxic side effects (data not shown).

Samples

Plasma samples and mouse lungs were obtained on months 2, 4, 6, 5, 9, and 12 after treatment. Representative lung lobes were ligated, sectioned, and rapidly frozen in liquid nitrogen. The remaining material was fixed by immersion in 4% formaldehyde for 24 hours, embedded in paraffin, sectioned along the main bronchial axis, and cut at 3- μ m thickness for immunohistochemical analysis.

At the time of analysis, 20- μ m thickness cryostat sections of the frozen lobe were obtained and lesions were microdissected by laser capture microdissection (Leica, Wezlar, Germany). RNA and DNA from microdissected tissues were extracted using RNeasy Kit (Qiagen, Valencia, CA) and DNA Mini Kit (Qiagen), respectively.

Lesion Analysis

Tumor incidence was assessed microscopically in a representative set of six sections per mouse including all of the lung lobes. Tumor areas were calculated using the formula: $A (\mu\text{m}^2) = \pi \times L \times W$, where L is the largest diameter and W is the largest diameter perpendicular to L . Tumors were classified as adenoma (solid or papillary) or adenocarcinoma, in accordance with the criteria previously published [20].

Cytokine Measurement

The concentrations of TNF- α , macrophage inflammatory protein-1 α (MIP-1 α), interferon gamma-induced protein 10 (IP-10), interleukin-1 beta (IL-1 β), IL-6, granulocyte-macrophage colony-stimulating factor (GM-CSF), IL-10, IL-13, interferon gamma (INF- γ), and IL-12 (p40) were determined in plasma using a mouse Milliplex MAP Kit (Millipore, Madrid, Spain) following the manufacturer's instructions.

Immunostaining

Immunostaining was performed using antibodies raised against mouse p-H2AX (1:50; Cell Signaling Technology, MA), mouse pro-SPC (1:500; Abcam, Cambridge, MA), CC10 (1:4000; Upstate, Billerica, MA), mouse Ki-67 (1:25; Neomarkers, Fremont, CA), mouse CD31 (1:40; Dianova, Hamburg, Germany), mouse cleaved caspase-3 (1:100; Cell Signaling Technology, Danvers, MA), mouse forkhead box P3 (FOXP3; 1:50; ebiosciences, Frankfurt, Germany), and Retnla (1:250; Abcam). Heat-mediated antigen retrieval was used for antibodies against Ki-67, CD31, cleaved caspase-3, FOXP3, and Retnla by microwave exposure for 15 minutes at 800 W and 15 minutes at 375 W in 10 mM sodium citrate (pH 6). Incubations with anti-CC10 and anti-Retnla antibodies were followed by incubation with the indirect avidin-biotin-peroxidase system (Dako, Barcelona, Spain). In the case of p-H2AX, pro-SPC, Ki-67, CD31, cleaved caspase-3, and FOXP3 immunostaining, Envision signal enhancement method (Dako) was used. Slides were washed in TBS and peroxidase activity was detected with 3,3'-diaminobenzidine (Dako). Slides were counterstained with Harris' hematoxylin. Omission of the primary antibodies was used as a negative control in one slide from each staining series. p-H2AX, pro-SPC, Ki-67, cleaved caspase-3, and FOXP3 immunostaining was evaluated by two independent and blinded observers and scored as the mean of the percentages of stained cells in 20 high-power fields ($\times 400$). Quantification of CD31 staining was calculated as the mean of the ratio between CD31-positive area and total area using the Analysis software (Olympus, Barcelona, Spain).

Immunohistochemistry to detect mouse CD4, CD8, CD3, CD20, myeloperoxidase, and CD68 was performed using FLEX Ready-to-Use specific antibodies (Dako) according to the manufacturer's conditions.

Mutation Analysis

Mutations in *K-RAS* (codons 12 and 61), *STK11* (exons 1-5, 8, and 9), and *TP53* (exons 5, 6, 7, 8, and 9) genes were analyzed in DNA from microdissected malignant tissues by polymerase chain reaction (PCR) amplification and sequencing. Genes were analyzed in DNA from microdissected malignant tissues. DNA was amplified by PCR using the primers shown in Table W1. After PCR amplification, exons upstream and downstream were sequenced using a BigDye Terminator 3.1 sequencing instrument (Applied Biosystems, Carlsbad, CA); sequences were then compared to a control sequence with SeqScape v2.5 (Applied Biosystems). When a mutation was detected, an additional amplification and sequencing experiment was performed to confirm the result.

Expression Arrays

Gene expression profiles were analyzed in 16 individual lesions (9 adenomas and 7 adenocarcinomas) from NDMA-silica-treated

mice and 10 individual lesions (5 adenomas and 5 adenocarcinomas) from NDMA-only-treated mice. RNA was obtained from microdissected tissue of at least eight consecutive 20- μ m sections from each frozen tissue block and retrotranscribed. Gene expression was analyzed using a microarray platform containing 28,122 mouse genes (Oryzon Genomics, Barcelona, Spain) following the manufacturer's instructions. For control, cDNA from normal lung was used in all hybridizations.

Normalization of every individual array was performed using the lowest scatterplot smoother implemented in Matlab software as previously described [21]. All of the probes of the array, aside from controls, were used for normalization; the fraction of the data used for smoothing at each point was set to 5%. After calculation of the fold change values, a filtering process was applied to eliminate low expression spots. The criterion of $|FC| > 2$ in at least one of the samples reduced the number of probes to 33,611 (corresponding to approximately 11,200 genes).

Statistics

Differences between two groups were analyzed using the Mann-Whitney U test. To determine differences between more than two experimentally independent groups, Kruskal-Wallis H test was chosen.

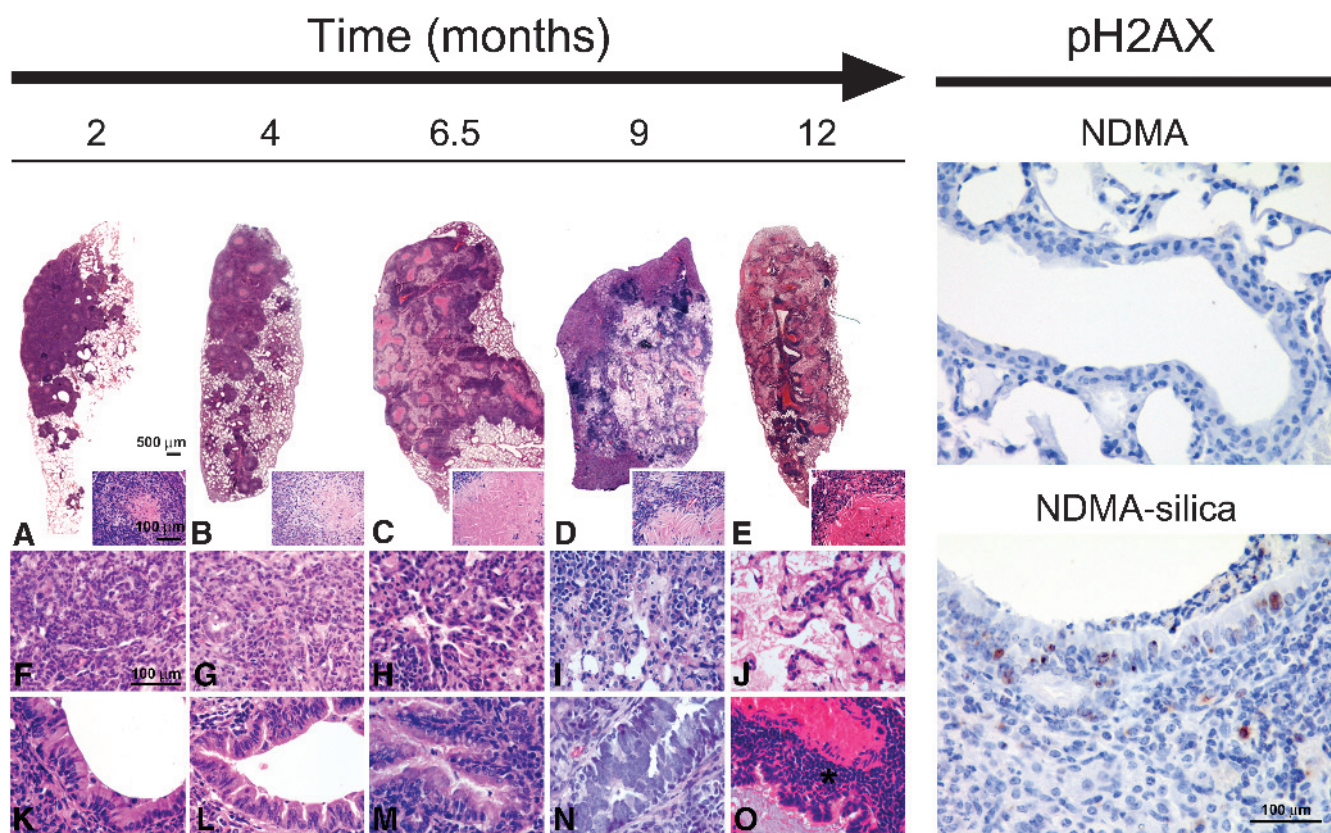


Figure 1. Effects of oropharyngeal administration of silica on mouse lungs. The left panel shows the histologic analysis of lung silica-induced chronic inflammation in sections stained with hematoxylin and eosin. Silica alone-treated mice were sacrificed at months 2 ($n = 4$), 4 ($n = 4$), 6.5 ($n = 4$), 9 ($n = 4$), and 12 ($n = 4$) after treatment. Lungs were harvested and all the lung lobes were analyzed (one field per lobe). (A–E) Silicotic granulomas at different experimental points following silica treatment. Insets show the details of the granulomatous proliferations. (F–O) Alveolar (F–J) and bronchiolar (K–O) hyperplasia in areas close to the granulomas at 2, 4, 6.5, 9, and 12 months after silica treatment. Alveolar proteinosis (J), hyperplastic goblet cells (N), and perivascular, peribronchiolar inflammatory reaction (asterisk, O) and lung fibrotic lesions (data not shown) are common features in this model. Images were obtained at the same magnification. The right panel includes representative examples of p-H2AX staining in lungs from NDMA-only- and NDMA-silica-treated mice. Samples were considered positive when six or more cells presented positive immunoreactivity in at least two of three fields analyzed ($\times 40$).

Table 1. Immunohistochemical Characterization of Leukocyte Infiltrate in Lungs from Mice Treated with NDMA, Silica, and NDMA-Silica.

Cell Type	Marker	Time (Months)	Treatment*			P Value†
			NDMA (Mean ± SD)‡	Silica (Mean ± SD)‡	NDMA-Silica (Mean ± SD)‡	
CD4 T lymphocytes	CD4	2	1.13 ± 0.95	5 ± 1.18	3.96 ± 0.8	.015
		4	1.04 ± 0.42	4.17 ± 1.18	4.38 ± 1.85	.022
		6.5	0.83 ± 0.68	3.73 ± 1.08	5 ± 1.52	.018
CD8 T lymphocytes	CD8	2	1.25 ± 0.48	8.75 ± 1.68	8.13 ± 1.72	.022
		4	1.04 ± 0.42	7.71 ± 1.42	8.13 ± 1.72	.022
		6.5	0.83 ± 0.68	6.88 ± 1.58	7.5 ± 1.8	.023
T lymphocytes	CD3	2	0.92 ± 0.55	7.71 ± 1.42	8.33 ± 0	.017
		4	1.25 ± 0.48	9.79 ± 3.87	7.5 ± 1.18	.02
		6.5	0.92 ± 0.7	10.42 ± 1.77	10.28 ± 3.15	.048
B lymphocytes	CD20	2	0 ± 0	1.88 ± 0.42	2.08 ± 0.48	.011
		4	0.21 ± 0.42	2.29 ± 0.42	3.75 ± 1.08	.001
		6.5	0.21 ± 0.42	3.33 ± 1.52	3.96 ± 0.42	.019
Polymorphonuclear leukocytes	Myeloperoxidase	2	0.11 ± 0.19	2.29 ± 0.83	1.92 ± 0.17	.032
		4	0.17 ± 0.19	2.92 ± 0.48	3.33 ± 1.18	.022
		6.5	0.17 ± 0.19	3.13 ± 0.42	3.75 ± 1.08	.022
Monocyte/macrophage	CD68	2	0.21 ± 0.42	2.5 ± 0.68	2.08 ± 0.48	.019
		4	0.21 ± 0.42	5.83 ± 2.26	7.71 ± 3.36	.016
		6.5	0.42 ± 0.48	10.28 ± 0.48	9.17 ± 0.96	.015

*Four mice per treatment were analyzed 2, 4, and 6.5 months, respectively.

†Kruskal-Wallis H test.

‡Data represent the average of the percentage of positive cells in six high-power fields (×10).

Chi-square test with Fisher correction was applied to study differences between mutational profiles.

Differential gene signatures in expression array experiments were identified using Linear Models for Microarray data [22]. Genes were selected as significant using a *B* statistic cutoff ($B > 0$). A threshold of $|Z| > 2.3$ (P value $< .01$) was chosen to select genes for further analysis. R/Bioconductor [23] was used for preprocessing and statistical analysis. Functional enrichment analysis of Gene Ontology (GO) categories was conducted using Database for Annotation, Visualization and Integral Discovery [24], and the biologic interpretation was complemented through use of Ingenuity Pathway Analysis (Ingenuity Systems, Redwood City, CA), in which the database includes manually curated and fully traceable data derived from literature sources.

Results

Silica Strongly Promotes an Inflammatory Process, DNA Damage, and Pulmonary Fibrosis in Mouse Lungs

We first performed a histologic evaluation of the inflammatory response in lungs from mice treated with silica (Figure 1, *A–O*). Lung chronic inflammation was confirmed 2, 4, 6.5, 9, and 12 months after treatment in all silica-treated mice irrespective of NDMA administration; moreover, time-dependent progression of inflammation was clearly observed. In particular, 2 months after silica administration, nodular silicotic granulomas accompanied by marked epithelial hyperplasia were found in central areas close to branching and terminal bronchioles in all lung lobes from all treated mice (Figure 1, *A, F*, and *K*). Four months after treatment, inflamed regions were observed in the same lung areas; however, the size of the lesions was markedly larger. Granulomas were confluent and included large acellular centers with peripheral infiltration of lymphocytes. Moderate bronchiolar hyperplasia and hyperplastic type II pneumocytes were also observed surrounding the silicotic lesions (Figure 1, *B, G*, and *L*). After 6.5

and 9 months, silicotic granulomas remained similar in size to those observed after 4 months and exhibited larger central necrotic areas. Parenchyma between silicotic nodules presented increased alveolar proteinosis and thickened alveolar septa; epithelial hyperplasia persisted in the vicinity as well as between the granulomas, and extensive areas of hyperplastic goblet cells were also observed. Interestingly, there was a marked increase of macrophages and lymphocytes in the perivascular and peribronchiolar areas in comparison to lesions at month 4 (Figure 1, *C, D, H, I, M*, and *N*). Granulomas at month 12 exhibited larger central necrotic areas. At this time point, the relative abundance of epithelial hyperplasia was reduced, whereas macrophages and lymphocytes persisted in perivascular and peribronchiolar areas (Figure 1, *E, J*, and *O*). To characterize the inflammatory infiltrate in lungs from NDMA-only-, silica-, and NDMA-silica-treated mice, the presence of CD4 and CD8 T lymphocytes, total T lymphocytes, B lymphocytes, polymorphonuclear leukocytes, and monocyte/macrophage cells was evaluated by immunohistochemistry 2, 4, and 6.5 months after treatment. All these cell populations were significantly increased in lungs from silica-treated mice irrespective of NDMA administration in all of the experimental time points analyzed (Table 1 and Figure W1). NDMA administration did not affect inflammatory structural phenotype and leukocyte infiltration in lungs from mice treated with both silica and saline. In addition to the histopathologic analysis, we measured TNF- α , MIP-1 α , IP-10, IL-1 β , IL-6, GM-CSF, IL-10, IL-13, INF- γ , and IL-12 (p40) plasma concentrations. According to previous findings [25], silica-treated mice presented significantly higher levels of the pro-inflammatory cytokines TNF- α , MIP-1 α , and IP-10 in comparison to the non-silica-treated counterparts. No significant differences in IL-1 β , IL-6, GM-CSF, IL-10, IL-13, INF- γ , and IL-12 (p40) plasma levels were found between experimental groups (Figure W2). However, we found a significant increase of mRNA expression of IL-6 and GM-CSF in lungs from NDMA-silica when compared to NDMA-only-treated mice 12 months after treatment, whereas no significant differences between both experimental groups were found for IL-1 β (Figure W3).

To further evaluate the effects of silica instillation in mouse lungs, we analyzed the phosphorylation of histone H2AX to indicate the level of silica-mediated DNA damage present within lung epithelial cells. One hundred percent of lungs from NDMA-silica-treated mice presented positive p-H2AX staining in hyperplastic areas from bronchiolar epithelium ($n = 6$; Figure 1, *right panel*). This percentage was reduced over time to 50% (month 4; $n = 8$) and 33% (month 6.5; $n = 3$) and disappeared after month 9 ($n = 18$). Interestingly, p-H2AX was only observed in hyperplastic tissue areas near to granulomatous areas. None of the lungs from NDMA-only-treated ($n = 28$) or saline-treated ($n = 20$) mice were positive for p-H2AX. These results indicate that silica promotes DNA damage in lungs. Another important consequence of silica instillation was, as previously described [19], the development of fibrotic areas extending to the peripheral and distal regions of the lung in all of the experimental time points (data not shown). As previously described [18], we did not detect adenomas nor adenocarcinomas in mice treated with silica alone.

Chronic Inflammation Increases the Incidence and Multiplicity of NDMA-Induced Lung Tumors

We next analyzed whether silica-mediated chronic lung inflammation influences the carcinogenic effects of NDMA. We examined the preneoplastic and neoplastic lesions in mice treated with saline, silica, a poorly tumorigenic dose of NDMA, and combination of the same

dose of NDMA and silica. Silica-treated mice developed chronic inflammation; however, no lung adenomas and adenocarcinomas were detected at any time during the experiment. However, 75% of mice treated with NDMA exhibited adenomas after 6.5 months. Pre-malignant adenomas were detected earlier in mice treated with the combination of silica and NDMA compared with NDMA-only-treated mice (4 months after treatment *vs* 6.5 months, respectively). Moreover, the incidence and multiplicity of these adenomas were markedly higher in all of the experimental time points in the combined treatment group compared with NDMA-only treatment (Figure 2A). Interestingly, mice treated with the combination of silica and NDMA also demonstrated a three-fold increase in both incidence and multiplicity of lung malignant adenocarcinomas compared with mice treated with NDMA only (Figure 2B). The ratios of adenocarcinoma to adenoma were statistically equivalent: 0.20 ± 0.3 in the combined treatment and 0.12 ± 0.27 in NDMA only ($P = .36$). Taken together, these data suggest that silica-mediated local chronic inflammation significantly reduces the latency period for the appearance of preneoplastic lung lesions and strongly promotes lung carcinogenesis.

Lesions in Mice Treated with NDMA and the Combination of NDMA with Silica Exhibit Similar Histologic and Molecular Features

Despite an increase in lung cancer incidence and multiplicity in mice treated with the combination of NDMA and silica, we did not observe

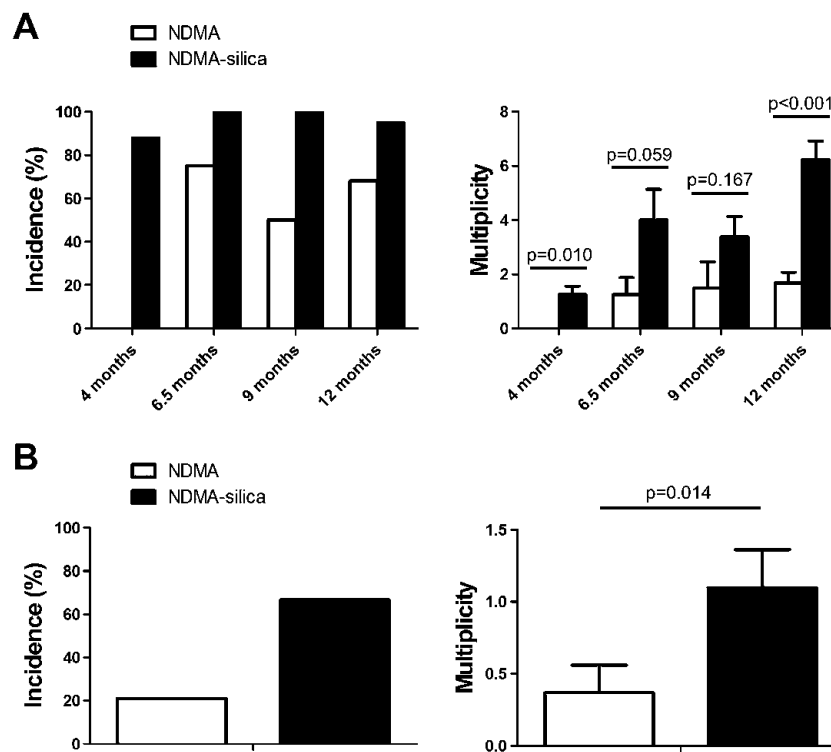


Figure 2. Incidence and multiplicity of adenomas and lung tumors in mice treated with NDMA-only or NDMA-silica. (A) Evaluation of adenomatous structures at different experimental time points. (B) Quantitation of adenocarcinomas at month 12 after treatment. NDMA-only-treated mice were analyzed at months 4 ($n = 4$), 6.5 ($n = 4$), 9 ($n = 4$), and 12 ($n = 19$) after treatment. NDMA-silica-treated mice were analyzed at months 4 ($n = 8$), 6.5 ($n = 8$), 9 ($n = 8$), and 12 ($n = 21$) after treatment. Incidence rate was calculated as the percentage of mice with at least one lung lesion. Multiplicity is represented as the average of the number of lesions found in mouse lungs \pm SEM. P values were calculated using the Kruskal-Wallis test in adenomas, whereas the test chosen for the analysis of adenocarcinomas was the Mann-Whitney U test.

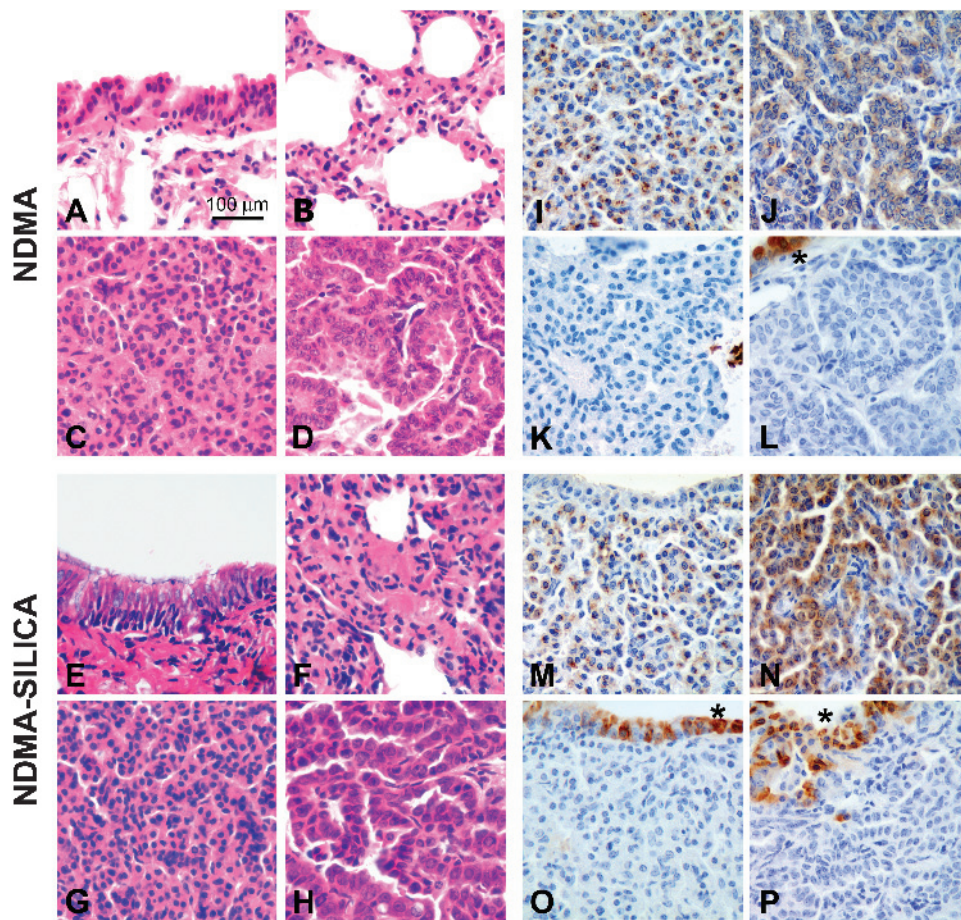


Figure 3. Histopathologic features of lung lesions from NDMA and NDMA-silica-treated mice. All lesions classified as adenomas and adenocarcinomas in Figure 2 were analyzed. (A–H) Hematoxylin and eosin staining of bronchiolar (A) and alveolar (B) epithelium, a solid adenoma (C), and a papillary adenocarcinoma (D) from NDMA-treated mice and bronchiolar hyperplasia (E), alveolar epithelium (F), a solid adenoma (G), and papillary adenocarcinoma (H) from NDMA-silica-treated mice. (I–P) Immunohistochemical analysis of pro-SPC and CC10 in tumors and adenomas from NDMA-silica- and NDMA-treated mice. Slides were counterstained with Harris' hematoxylin. All adenomas (I, M) and adenocarcinomas (J, N) exhibited positive staining for pro-SPC in both NDMA-silica- and NDMA-treated mice. Adenomas (K, O) and adenocarcinomas (L, P) were negative for CC10 staining in both experimental groups, whereas normal bronchiolar epithelial cells close to the tumors (*) exhibited CC10 positive staining. Scale bar, 100 μ m.

significant histologic differences between the lesions present in the two experimental groups (Figure 3, A–H). Immunohistochemical analysis of the expression of CC10, an airway Clara cell marker, and pro-SPC, a type II pneumocyte marker, revealed that adenomas and adenocarcinomas from NDMA-only- and NDMA-silica-treated mice were consistently positive for pro-SPC and negative for CC10, whereas non-malignant normal and hyperplastic bronchiolar epithelium exhibited positive staining for CC10, and only hyperplastic alveoli were positive for pro-SPC (Figure 3, I–P). These data suggest that tumors are potentially derived from hyperplastic type II cells or less committed cells following the type II differentiation pathway. Furthermore, we found no statistical differences in the average size of adenomas ($P = .405$) or adenocarcinomas ($P = .256$) between both experimental groups. Immunohistochemical analysis of Ki-67 and CD31 revealed that there was no increase in the proliferative capacity and in the vascular density of adenomas from NDMA-silica when compared to NDMA-only-treated mice. However, a statistically significant increase of active caspase-3 immunostaining was found in adenomas from NDMA-silica-treated mice when compared to those from NDMA-only-

treated mice ($P < .001$), suggesting that silica promotes apoptosis within adenomas (Figure W4).

Silica-mediated Chronic Inflammation Modifies the K-RAS Mutation Profile in NDMA-Induced Lung Tumors

We next evaluated the presence of somatic mutations in oncogenes and tumor suppressor genes associated with lung carcinogenesis in humans and mice: *K-RAS*, *STK11*, and *p53*. In particular, we analyzed activating mutations in *K-RAS* (codons 12 and 61) and inactivating mutations in *TP53* (exons 5–9) and *STK11* (exons 1–5, 8, and 9). This analysis was performed on DNA from lung adenocarcinomas of mice treated with NDMA-silica ($n = 10$) or NDMA only ($n = 5$). Of the 15 adenocarcinomas studied, 13 exhibited mutation in *K-RAS*, either in codon 12 or codon 61. Importantly, the mutational pattern was different between the NDMA-only and NDMA-silica-induced lesions. Specifically, the *K-RAS* mutations in tumors that originated following NDMA-silica treatment was primarily G-to-A transition (G12D) in codon 12, whereas A-to-G transition (Q61R) in codon 61 was the most

frequent alteration in adenocarcinomas from mice treated with NDMA only ($P = .031$; Figure 4). None of the adenocarcinomas analyzed presented somatic mutations in *p53* and *STK11* hotspots.

Silica-induced Chronic Inflammation Exhibits a Pro-inflammatory Gene Expression Profile

To further characterize the effects of silica-mediated chronic inflammation in lung carcinogenesis, we performed microarray analysis. Minimal differences in gene expression were found in adenocarcinomas from NDMA-silica- and NDMA-only-treated mice (Table W2). However, marked gene expression differences were observed between NDMA-silica and NDMA-only adenomas. In particular, 36 genes were upregulated and 13 downregulated in adenomas from mice treated with NDMA-silica compared to mice treated with NDMA only (Figure 5A and Table 2). Interestingly, a substantial group of the most relevant upregulated genes in the NDMA-silica model, such as *Saa3*, *Retnla*, *Irg1*, *Serpina3n*, *Adam8*, and *Lta*, plays a key role in inflammation. To confirm this finding at the protein level, we chose one of these genes, *Retnla*, upon commercial availability of commercial anti-mouse specific protein antibody. *Retnla* expression was analyzed by immunohistochemistry (Figure 5B). Most of the adenomas (17 of 23) from NDMA-silica-treated mice exhibited positive staining for *Retnla*, whereas adenomas (11 of 16) from NDMA-only-treated mice were negative ($P = .011$). Functional analysis of the genes differentially expressed in adenomas and adenocarcinomas from both experimental groups demonstrated differences in the enriched GO categories. In adenomas, the presence of silica-mediated inflammation affected GO categories associated with inflammation and immune response, whereas enriched categories in adenocarcinomas were unrelated to these processes (Table W3).

Silica-induced Chronic Inflammation Promotes an Immunosuppressive Microenvironment in Adenomas

Malignant transformation may be associated with an immunosuppressive microenvironment. Using microarray expression data, we analyzed whether silica-induced chronic inflammation generates an immunosuppressive microenvironment in adenomas and adenocarcinomas in NDMA-treated mice (Figure 6). Genes associated with immunosuppression, such as PD-1, transforming growth factor- β 1 (TGF- β 1), lymphocyte-activation gene 3 (LAG3), monocyte chemoattractant protein 1 (MCP-1), or FOXP3, presented higher expression

levels in adenomas from NDMA-silica-treated mice compared to mice treated with NDMA only (Figure 6A). No differences were observed in the expression of these genes among adenocarcinomas from both experimental groups (data not shown). Additionally, we assessed the presence of FOXP3-positive cells within adenomas from mice treated with NDMA-silica ($n = 15$) and NDMA only ($n = 15$) using immunohistochemistry. All FOXP3-positive cells analyzed presented lymphocyte morphology. Positive FOXP3-positive lymphocytes were counted separately in the lesions and in the immediate peripheral lung parenchyma tissue (the "capsule" of the lesion). We did not observe FOXP3-positive lymphocytes within adenomas from NDMA-only-treated mice, whereas 7.1% of adenomas from NDMA-silica-treated mice exhibited at least one FOXP3-positive lymphocyte (Figure 6B). We analyzed the FOXP3-positive cells present at the periphery of adenomas; one hundred percent of adenomas from NDMA-silica-treated mice exhibited at least one FOXP3-positive peripheral lymphocyte, whereas only 16.5% of adenomas generated following NDMA-only treatment exhibited at least one FOXP3-positive lymphocyte in the peritumoral area (Figure 6B).

Finally, we investigated whether silica-induced chronic inflammation increases the number of FOXP3-positive lymphocytes in distant lung tissue. We analyzed the presence of FOXP3-positive lymphocytes in lymphoid clusters located in non-injured lung areas distant from adenomas. Twelve percent of NDMA-silica lymphocytes stained positive for FOXP3 in these distant clusters, whereas only 2.7% were positive in the NDMA treatment (Figure 6, C and D). Taken together, these results demonstrate that silica-mediated chronic inflammation promotes the development of an immunosuppressive microenvironment.

Discussion

In this study, we demonstrated that chronic inflammation strongly promotes lung carcinogenesis in mice. To mimic human lung cancer in the context of chronic inflammation, we developed for the first time a chemical-induced carcinogenesis mouse model that comprised the administration of a low tumorigenic dose of NDMA, a carcinogen present in tobacco smoke, in the presence of chronic silica-induced lung inflammation. Silica is a particulate irritant that induces pulmonary inflammation in a similar way as other inhaled particles, such as asbestos [26]. In our study, histologic analysis of the lungs from silica-treated mice revealed that, as previously described

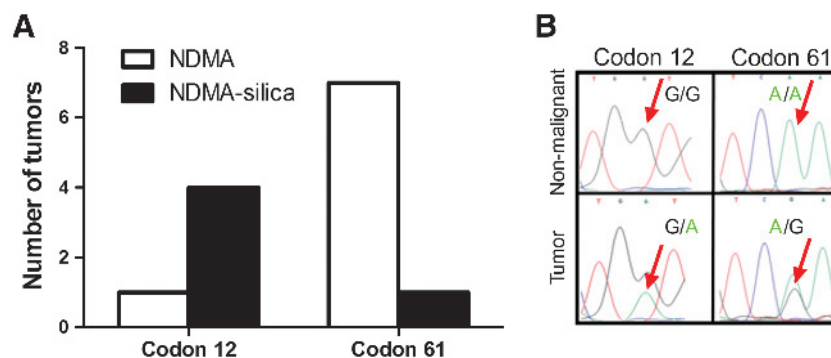


Figure 4. *K-RAS* mutational analysis of adenocarcinomas from the NDMA-silica- and NDMA-only-treated mice. (A) Total number of adenocarcinomas with either *K-RAS* codon 12 or 61 mutations in NDMA-silica- and NDMA-treated mice. (B) Representative electropherograms showing G-to-A transition in *K-RAS* codon 12 and A-to-G transition in codon 61. Differences between groups were analyzed using the Fisher exact test.

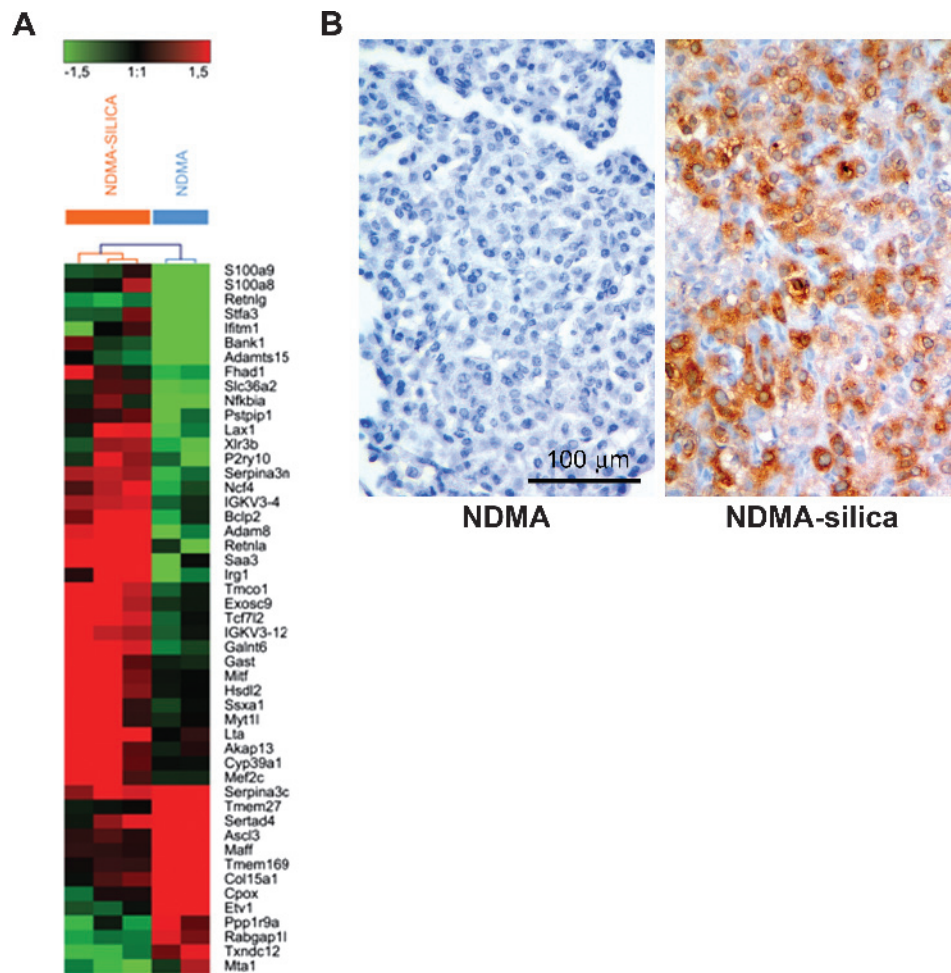


Figure 5. Differentially expressed genes after a comparison of gene expression profiles of adenomas from NDMA and NDMA-silica-treated mice. (A) Matrix expression of the representative signature for the set of genes differentially expressed ($B > 0$; $|\log FC| > 1.5$). Each line represents the gene expression profile of a mixture of RNA from at least two different adenomas (total $n = 14$). Red and green represent upregulated and downregulated genes, respectively, when compared to the corresponding normal lung tissue expression profile. (B) Retnla negative staining in an NDMA adenoma (left panel) and Retnla positive staining in an NDMA-silica adenoma located close to silica-induced lung inflammation (right panel). Retnla staining was performed in adenomas from 10 mice treated with NDMA and 16 mice treated with NDMA-silica. Differences between groups were analyzed using the Fisher exact test.

[25,27], this compound triggers a chronic and progressive granulomatous lung inflammation accompanied by a systemic increase of pro-inflammatory cytokines TNF- α , IP-10, and MIP-1 α . Importantly, the analysis of the model at different experimental time points allowed us to explore in depth preneoplastic and full malignant neoplastic lesions. Thus, we found that silica-induced chronic lung inflammation markedly increases the incidence and multiplicity of lung adenomas and adenocarcinomas following NDMA treatment. These results are in concordance with other animal models that explore the effects of different inflammatory agents in chemically induced lung tumor promotion. Continuous administration of butylated hydroxytoluene has been shown to increase the carcinogenic effects of both 3-methylcholanthrene [28] and urethane [29]. Exposure to a lysate of *Haemophilus influenzae*, an agent that triggers chronic obstructive pulmonary disease-like airway inflammation, has also been reported to generate a higher incidence of lung tumors [30]. It has also been demonstrated that inflammation caused by repetitive exposure to specific levels of tobacco smoke increases carcinogenesis in both carcinogen-treated mice and in conditional *K-RAS* transgenic mice [31].

Chemicals such benzo[a]pyrene, benz[*j*]aceanthrylene, cyclopenta[*cd*]pyrene, and 3-methylcholanthrene promote *K-RAS* point mutations in codons 12 and 13, whereas the predominant mutation in ethyl carbamate- and urethane-induced lung tumors occurs in codon 61 [32–36]. In the present study, our findings indicated that in lung adenocarcinomas from mice treated with NDMA only, glutamine in codon 61 is replaced by arginine. However, adenocarcinomas generated in a silica-mediated inflammation context exhibit G-to-A transition in codon 12. Interestingly, activation of *K-RAS* through transition G12D mutation is strongly associated with the presence of marked inflammation characterized by the production of inflammatory chemokines and infiltration of alveolar macrophages and lymphocytes [37]. In human lung tumors, the most frequent *K-RAS* gene alterations are point mutations in codon 12 [38]. Thus, the pattern of *K-RAS* mutations in human lung cancer is more similar to the combined NDMA-silica model compared to the NDMA-only model. None of the adenocarcinomas analyzed exhibited somatic mutations in TP53 or *STK11*; the absence of TP53 mutations is common in chemically induced mouse tumors [39].

The development of an immunosuppressive microenvironment seems very relevant for malignant transformation and is closely associated with chronic inflammation [7]. We did not observe differences in the presence of immunosuppressive genes between adenocarcinomas from NDMA-only- *versus* NDMA-silica-treated mice. In contrast, there were clear differences in the expression of the immunosuppressive genes PD-1, TGF- β 1, MCP-1, LAG3, and FOXP3. PD-1 is an immunosuppressor membrane protein present on activated T cells. The clinical usefulness of PD-1 blockade by a specific antibody has recently been demonstrated in patients with advanced non-small cell lung cancer [14]. TGF- β 1 modulates processes such as cell invasion or immune regulation and thus avoids the protumorigenic effects of chronic inflammation [40]. Interestingly, blockade of the activity of TGF- β 1 by neutralizing antibodies inhibits lung metastasis in mice [41]. MCP-1 is a chemokine locally produced by tumors and involved

in the recruitment of inflammatory cells. A high level of MCP-1 promotes tumor macrophage infiltration and correlates with poor prognosis and metastatic disease in patients with breast cancer [42]. Inhibition of MCP-1 significantly improves tumor immunotherapy [43]. Furthermore, these factors (PD-1, TGF- β 1, and MCP-1) also exert immunosuppressive activities through the promotion of Tregs activities [43–45]. Tregs are produced in the thymus as a functionally mature T cell subpopulation [46]. They are important in maintaining immune tolerance and limiting autoimmunity. However, Tregs also attenuate immune responses against tumors [47,48]. In fact, the suppressive activity and number of Tregs are increased in human lung cancer [49,50]. LAG3 and FOXP3 are two important markers of Tregs. LAG3 is a CD4-related protein that binds major histocompatibility complex (MHC) class II and reduces the proliferation of T cells [51]. FOXP3 is a key regulator of the development and function of

Table 2. Genes Differentially Expressed in Adenomas from NDMA-Silica-Treated Mice *versus* Adenomas from NDMA-Treated Mice ($B = 0$; $|\log FC| \geq 1.5$).

Genes	Description	Log FC	P Value	B
Upregulated genes				
<i>Saa3</i>	Serum amyloid A 3	3.95	.000131	1.15
<i>Tcf7l2</i>	Transcription factor 7-like 2, T cell specific	3.63	.000109	1.32
<i>S100a8</i>	S100 calcium binding protein A8 (calgranulin A)	3.63	.000001	5.08
<i>Retnla</i>	Resistin-like α	3.50	.000015	3.04
<i>Irg1</i>	Immunoresponsive gene 1	3.38	.000434	0.10
<i>S100a9</i>	S100 calcium binding protein A9 (calgranulin B)	3.25	.000009	3.49
<i>Tmco1</i>	Transmembrane and coiled-coil domains 1	3.11	.000196	0.80
<i>Exosc9</i>	Exosome component 9	3.05	.000415	0.14
<i>Adam8</i>	A disintegrin and metallopeptidase domain 8	2.93	.000051	1.97
<i>Gast</i>	Gastrin	2.48	.000291	0.45
<i>Sfta3</i>	Stefin A3	2.43	.000126	1.19
<i>Bclp2</i>	Chitinase-like protein 2	2.33	.000462	0.05
<i>Mitf</i>	Microphthalmia-associated transcription factor	2.32	.000117	1.25
<i>Hsd12</i>	Hydroxysteroid dehydrogenase like 2	2.23	.000348	0.30
<i>Ssxa1</i>	Synovial sarcoma, X member A, breakpoint 1	2.22	.000319	0.37
<i>Lta</i>	Lymphotoxin A	2.14	.000342	0.31
<i>Ifitm1</i>	Interferon-induced transmembrane protein 1	2.13	.000376	0.23
<i>Lax1</i>	Lymphocyte transmembrane adaptor 1	2.11	.000244	0.61
<i>Galnt6</i>	UDP-N-acetyl- α -D-galactosamine:polypeptide N-acetylgalactosaminyltransferase 6	2.08	.000012	3.20
<i>Myt1l</i>	Myelin transcription factor 1-like	2.07	.000468	0.03
<i>Retnlg</i>	Resistin-like γ	1.98	.000043	2.13
<i>Adams15</i>	A disintegrin-like and metallopeptidase (reprolysin type) with thrombospondin type 1 motif, 15	1.96	.000070	1.70
<i>Bank1</i>	B-cell scaffold protein with ankyrin repeats 1	1.96	.000043	2.13
<i>Mef2c</i>	Myocyte enhancer factor 2C	1.94	.000340	0.32
<i>Serpina3n</i>	Serine (or cysteine) peptidase inhibitor, clade A, member 3N	1.89	.000014	3.12
<i>Akap13</i>	A kinase (PRKA) anchor protein 13	1.84	.000226	0.68
<i>IGKV3-12</i>	Immunoglobulin κ light chain V gene segment	1.79	.000041	2.16
<i>Nfkb1a</i>	Nuclear factor of κ light chain gene enhancer in B-cells inhibitor, α	1.72	.000090	1.48
<i>P2ry10</i>	Purinergic receptor P2Y, G-protein coupled 10	1.70	.000123	1.21
<i>Ncf4</i>	Neutrophil cytosolic factor 4	1.68	.000306	0.41
<i>Cyp39a1</i>	Cytochrome P450, family 39, subfamily a, polypeptide 1	1.67	.000257	0.56
<i>Xlr3b</i>	X-linked lymphocyte-regulated 3B (Source: MarkerSymbol;Acc:MGI:109505)	1.67	.000459	0.05
<i>Slc36a2</i>	Solute carrier family 36 (proton/amino acid symporter), member 2	1.66	.000075	1.64
<i>Pstpip1</i>	Proline-serine-threonine phosphatase-interacting protein 1	1.59	.000139	1.10
<i>IGKV3-4</i>	Immunoglobulin κ light chain V gene segment	1.52	.000020	2.78
<i>Fhda1</i>	Forkhead-associated (FHA) phosphopeptide binding domain 1	1.52	.000365	0.25
Downregulated genes				
<i>Tmem169</i>	Transmembrane protein 169	-1.51	.000281	0.48
<i>Mta1</i>	Metastasis associated 1	-1.63	.000379	0.22
<i>Ppp1r9a</i>	Protein phosphatase 1, regulatory (inhibitor) subunit 9A	-1.72	.000396	0.18
<i>Ascl3</i>	Achaete-scute complex homolog-like 3 (Drosophila)	-1.74	.000317	0.38
<i>Col15a1</i>	Procollagen, type XV	-1.75	.000425	0.12
<i>Maff</i>	V-maf musculoaponeurotic fibrosarcoma oncogene family, protein F (avian)	-1.78	.000225	0.68
<i>Rabgap11</i>	RAB GTPase activating protein 11-like	-1.78	.000018	2.88
<i>Etv1</i>	Ets variant gene 1	-2.04	.000038	2.24
<i>Txndc12</i>	Thioredoxin domain containing 12 (endoplasmic reticulum)	-2.05	.000275	0.50
<i>Cpx</i>	Coproporphyrinogen oxidase	-2.40	.000025	2.59
<i>Serpina3c</i>	Serine (or cysteine) peptidase inhibitor, clade A, member 3C	-2.82	.000158	0.99
<i>Sertad4</i>	SERTA domain containing 4	-2.89	.000012	3.24
<i>Tmem27</i>	Transmembrane protein 27	-3.18	.000049	2.01

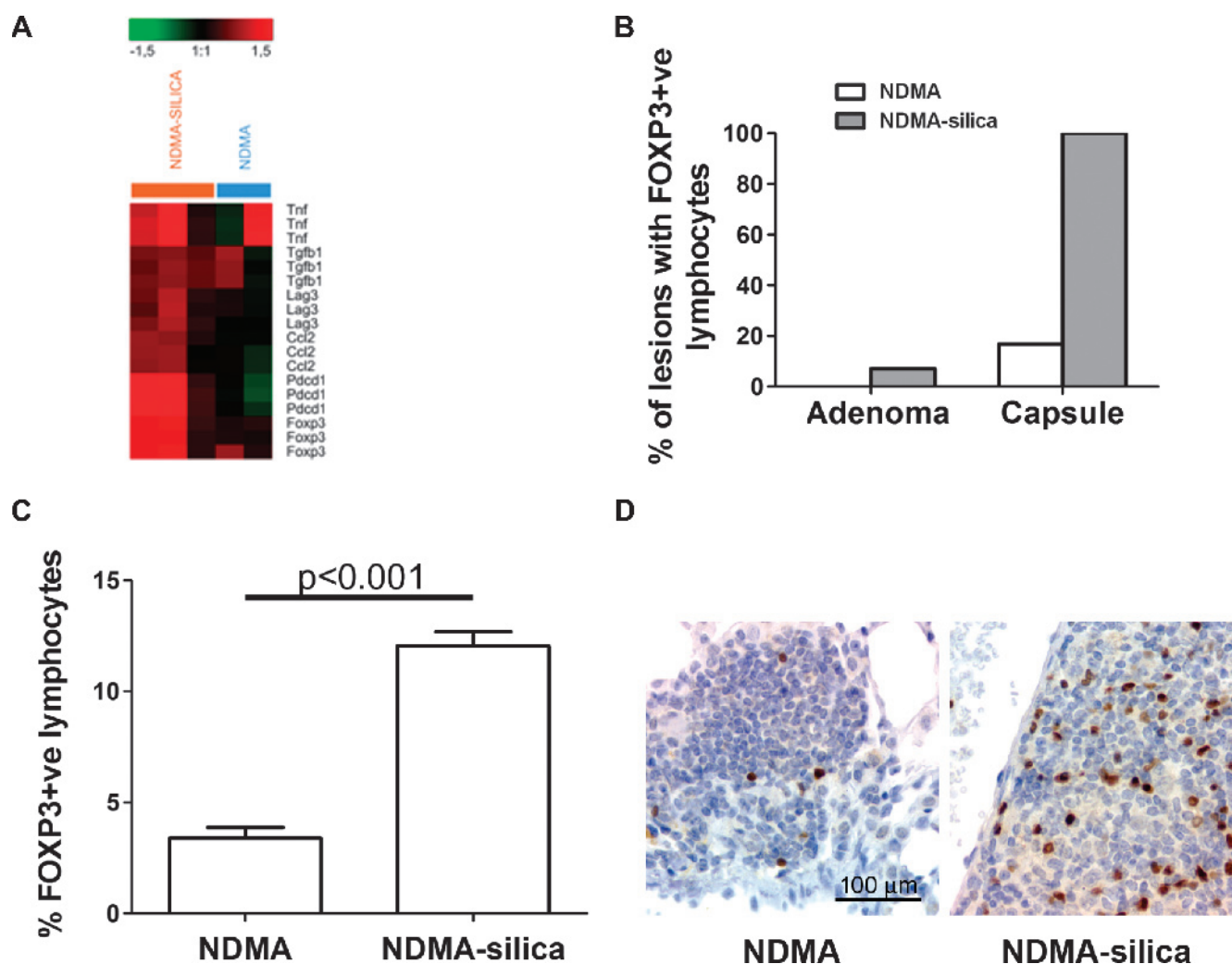


Figure 6. Expression of different immunomodulators in adenomas from NDMA-silica- and NDMA-treated mice. (A) Signature of immunosuppressive genes expressed in adenomas from NDMA-silica-treated mice compared to NDMA-treated mice. Each line represents the gene expression profile of a mixture of RNA from at least two different adenomas (total $n = 14$). Upregulated and downregulated genes are shown in red and green, respectively. (B) Percentage of lesions with FOXP3-positive cells within adenomas and adenoma peripheral areas ("capsule") from NDMA-silica-treated ($n = 15$) and NDMA-treated ($n = 15$) mice. (C) Percentage of FOXP3-positive lymphocytes to total lymphocytes counted on lymphoid clusters located in non-injured lung parenchyma areas from NDMA-silica- and NDMA-treated mice. Values are represented as the means \pm SEM. (D) FOXP3 immunohistochemical staining of lymphoid clusters from NDMA- and NDMA-silica-treated mice. The P value was calculated using the Mann-Whitney U test.

Tregs [52]. In accordance with previous studies [53], we have found an increase in the percentage of FOXP3-positive lymphocytes in lymphoid clusters in mice treated with silica. Importantly, we found a marked increase of Tregs in preneoplastic lesions in NDMA-silica-treated mice. The permissive environment provided by FOXP3-positive T cells is required for *K-RAS*-mediated tumorigenesis in mice treated with 4-(*N*-nitrosomethylamino)-1-(3-pyridyl)-1-butanone, a carcinogen present in tobacco smoke [54]. In addition to promoting an immunosuppressive microenvironment, silica-induced chronic inflammation significantly increased apoptosis levels within adenomas maybe due to the increased DNA damage and the inflammatory stress triggered by silica administration. Taken together, our findings suggest that chronic inflammation generates a favorable microenvironment for the generation of preneoplastic lesions that potentially contributes to the progression of adenomas to adenocarcinomas.

In summary, in this study, we developed a novel mouse model of lung cancer that allows for the study of the interaction of chronic

inflammation with lung tumorigenesis. Molecular analysis of this model reveals some of the underlying mechanisms through which chronic inflammation facilitates the development of preneoplastic lesions and, consequently, lung cancer. Elucidation of the interplay between inflammation and lung carcinogenesis will help in the development of preventive strategies to slow down or avoid the generation of premalignant lesions and the conversion to malignant tumors.

Acknowledgments

This paper is dedicated to the memory of Prof Alvin M. Malkinson who played a major role in the field of inflammation and lung carcinogenesis in mouse models. His findings profoundly influenced the present publication. We are also very grateful to Prof Umberto Saffiotti for his key contributions to the field of silica-induced lung carcinogenesis and his help in our initial efforts to set up silica-induced rodent tumor models. We also thank Cristina Sainz for technical support.

References

- [1] Jemal A, Siegel R, Ward E, Hao Y, Xu J, and Thun MJ (2009). Cancer statistics, 2009. *CA Cancer J Clin* **59**, 225–249.
- [2] Boffetta P (2004). Epidemiology of environmental and occupational cancer. *Oncogene* **23**, 6392–6403.
- [3] Donaldson K and Poland CA (2012). Inhaled nanoparticles and lung cancer—what we can learn from conventional particle toxicology. *Swiss Med Wkly* **142**, w13547.
- [4] Houghton AM, Mouded M, and Shapiro SD (2008). Common origins of lung cancer and COPD. *Nat Med* **14**, 1023–1024.
- [5] Xu J, Yin Z, Gao W, Liu L, Wang R, Huang P, Yin Y, Liu P, Yu R, and Shu Y (2012). Meta-analysis on the association between nonsteroidal anti-inflammatory drug use and lung cancer risk. *Clin Lung Cancer* **13**, 44–51.
- [6] Dannenberg AJ and Subbaramaiah K (2003). Targeting cyclooxygenase-2 in human neoplasia: rationale and promise. *Cancer Cell* **4**, 431–436.
- [7] de Visser KE, Eichten A, and Coussens LM (2006). Paradoxical roles of the immune system during cancer development. *Nat Rev Cancer* **6**, 24–37.
- [8] Wistuba II and Gazdar AF (2006). Lung cancer preneoplasia. *Annu Rev Pathol* **1**, 331–348.
- [9] Hanahan D and Weinberg RA (2011). Hallmarks of cancer: the next generation. *Cell* **144**, 646–674.
- [10] Du C and Wang Y (2009). The immunoregulatory mechanisms of carcinoma for its survival and development. *J Exp Clin Cancer Res* **30**, 12.
- [11] Melief CJ (2008). Cancer immunotherapy by dendritic cells. *Immunity* **29**, 372–383.
- [12] Sinha P, Clements VK, Bunt SK, Albelda SM, and Ostrand-Rosenberg S (2007). Cross-talk between myeloid-derived suppressor cells and macrophages subverts tumor immunity toward a type 2 response. *J Immunol* **179**, 977–983.
- [13] Brahmer JR, Tykodi SS, Chow LQ, Hwu WJ, Topalian SL, Hwu P, Drake CG, Camacho LH, Kauh J, Odunsi K, et al. (2012). Safety and activity of anti-PD-L1 antibody in patients with advanced cancer. *N Engl J Med* **366**, 2455–2465.
- [14] Topalian SL, Hodi FS, Brahmer JR, Gettinger SN, Smith DC, McDermott DF, Powderly JD, Carvajal RD, Sosman JA, Atkins MB, et al. (2012). Safety, activity, and immune correlates of anti-PD-1 antibody in cancer. *N Engl J Med* **366**, 2443–2454.
- [15] Farago AF, Snyder EL, and Jacks T (2012). SnapShot: Lung cancer models. *Cell* **149**, 246–246.e1.
- [16] Griivennikov SI, Greten FR, and Karin M (2010). Immunity, inflammation, and cancer. *Cell* **140**, 883–899.
- [17] Leung CC, Yu IT, and Chen W (2012). Silicosis. *Lancet* **379**, 2008–2018.
- [18] Castranova V, Wallace WE, and Vallyathan V (1995). *Silica and Silica-Induced Lung Diseases*. Informa Healthcare, CRC, Boca Raton, FL.
- [19] Lakatos HF, Burgess HA, Thatcher TH, Redonnet MR, Hernady E, Williams JP, and Sime PJ (2006). Oropharyngeal aspiration of a silica suspension produces a superior model of silicosis in the mouse when compared to intratracheal instillation. *Exp Lung Res* **32**, 181–199.
- [20] Nikitin AY, Alcaraz A, Anver MR, Bronson RT, Cardiff RD, Dixon D, Fraire AE, Gabrielson EW, Gunning WT, and Haines DC (2004). Classification of proliferative pulmonary lesions of the mouse: recommendations of the mouse models of human cancers consortium. *Cancer Res* **64**, 2307–2316.
- [21] Yang YH, Dudoit S, Luu P, and Speed TP (2001). Normalization for cDNA microarray data. In *Microarrays: Optical Technologies and Informatics*. ML Bittner, Y Chen, AN Dorsel, and ER Dougherty (Eds). SPIE Press, Bellingham, WA. Vol. 4266 of Proceedings of SPIE.
- [22] Smyth GK (2004). Linear models and empirical bayes methods for assessing differential expression in microarray experiments. *Stat Appl Genet Mol Biol* **3**, 46–69; Article 3.
- [23] Gentleman R, Carey V, Huber W, Irizarry R, and Dudoit S (2005). *Bioinformatics and computational biology solutions using R and bioconductor*. Springer, New York, NY. pp. 49–69.
- [24] Huang da W, Sherman BT, and Lempicki RA (2009). Systematic and integrative analysis of large gene lists using DAVID bioinformatics resources. *Nat Protoc* **4**, 44–57.
- [25] Pryhuber GS, Huyck HL, Baggs R, Oberdorster G, and Finkelstein JN (2003). Induction of chemokines by low-dose intratracheal silica is reduced in TNFR1 (p55) null mice. *Toxicol Sci* **72**, 150–157.
- [26] Matsuzaki H, Maeda M, Lee S, Nishimura Y, Kumagai-Takei N, Hayashi H, Yamamoto S, Hatayama T, Kojima Y, Tabata R, et al. (2012). Asbestos-induced cellular and molecular alteration of immunocompetent cells and their relationship with chronic inflammation and carcinogenesis. *J Biomed Biotechnol* **2012**, 492608.
- [27] Driscoll KE, Lindenschmidt RC, Maurer JK, Higgins JM, and Ridder G (1990). Pulmonary response to silica or titanium dioxide: inflammatory cells, alveolar macrophage-derived cytokines, and histopathology. *Am J Respir Cell Mol Biol* **2**, 381–390.
- [28] Malkinson AM, Koski KM, Evans WA, and Festing MF (1997). Butylated hydroxytoluene exposure is necessary to induce lung tumors in BALB mice treated with 3-methylcholanthrene. *Cancer Res* **57**, 2832–2834.
- [29] Bojan F, Nagy A, and Herman K (1978). Effect of butylated hydroxytoluene and paraquat on urethan tumorigenesis in mouse lung. *Bull Environ Contam Toxicol* **20**, 573–576.
- [30] Barta P, Van Pelt C, Men T, Dickey BF, Lotan R, and Moghaddam SJ (2012). Enhancement of lung tumorigenesis in a *Gprc5a* Knockout mouse by chronic extrinsic airway inflammation. *Mol Cancer* **11**, 4.
- [31] Takahashi H, Ogata H, Nishigaki R, Broide DH, and Karin M (2010). Tobacco smoke promotes lung tumorigenesis by triggering IKK β - and JNK1-dependent inflammation. *Cancer Cell* **17**, 89–97.
- [32] Mass MJ, Jeffers AJ, Ross JA, Nelson G, Galati AJ, Stoner GD, and Nesnow S (1993). Ki-ras oncogene mutations in tumors and DNA adducts formed by benz[*a*]aceanthrylene and benzo[*a*]pyrene in the lungs of strain A/J mice. *Mol Carcinog* **8**, 186–192.
- [33] You M, Candrian U, Maronpot RR, Stoner GD, and Anderson MW (1989). Activation of the Ki-ras protooncogene in spontaneously occurring and chemically induced lung tumors of the strain A mouse. *Proc Natl Acad Sci USA* **86**, 3070–3074.
- [34] Nesnow S, Ross JA, Nelson G, Wilson K, Roop BC, Jeffers AJ, Galati AJ, Stoner GD, Sangaiah R, Gold A, et al. (1994). Cyclopenta[*cd*]pyrene-induced tumorigenicity, Ki-ras codon 12 mutations and DNA adducts in strain A/J mouse lung. *Carcinogenesis* **15**, 601–606.
- [35] Nuzum EO, Malkinson AM, and Beer DG (1990). Specific Ki-ras codon 61 mutations may determine the development of urethan-induced mouse lung adenomas or adenocarcinomas. *Mol Carcinog* **3**, 287–295.
- [36] Wessner LL, Fan M, Schaeffer DO, McEntee MF, and Miller MS (1996). Mouse lung tumors exhibit specific Ki-ras mutations following transplacental exposure to 3-methylcholanthrene. *Carcinogenesis* **17**, 1519–1526.
- [37] Ji H, Houghton AM, Mariani TJ, Perera S, Kim CB, Padera R, Tonon G, McNamara K, Marconcini LA, Hezel A, et al. (2006). K-ras activation generates an inflammatory response in lung tumors. *Oncogene* **25**, 2105–2112.
- [38] Okudela K, Woo T, and Kitamura H (2010). KRAS gene mutations in lung cancer: particulars established and issues unresolved. *Pathol Int* **60**, 651–660.
- [39] Hegi ME, Soderkvist P, Foley JF, Schoonhoven R, Swenberg JA, Kari F, Maronpot R, Anderson MW, and Wiseman RW (1993). Characterization of p53 mutations in methylene chloride-induced lung tumors from B6C3F1 mice. *Carcinogenesis* **14**, 803–810.
- [40] Massague J (2008). TGF β in cancer. *Cell* **134**, 215–230.
- [41] Biswas S, Guix M, Rinehart C, Dugger TC, Chytil A, Moses HL, Freeman ML, and Arteaga CL (2007). Inhibition of TGF- β with neutralizing antibodies prevents radiation-induced acceleration of metastatic cancer progression. *J Clin Invest* **117**, 1305–1313.
- [42] Qian BZ, Li J, Zhang H, Kitamura T, Zhang J, Campion LR, Kaiser EA, Snyder LA, and Pollard JW (2011). CCL2 recruits inflammatory monocytes to facilitate breast-tumour metastasis. *Nature* **475**, 222–225.
- [43] Fridlender ZG, Buchlis G, Kapoor V, Cheng G, Sun J, Singhal S, Crisanti MC, Wang LC, Heitjan D, Snyder LA, et al. (2010). CCL2 blockade augments cancer immunotherapy. *Cancer Res* **70**, 109–118.
- [44] Ni L, Ma CJ, Zhang Y, Nandakumar S, Zhang CL, Wu XY, Borthwick T, Hamati A, Chen XY, Kumaraguru U, et al. (2011). PD-1 modulates regulatory T cells and suppresses T-cell responses in HCV-associated lymphoma. *Immunol Cell Biol* **89**, 535–539.
- [45] Marie JC, Letterio JJ, Gavin M, and Rudensky AY (2005). TGF- β 1 maintains suppressor function and Foxp3 expression in CD4⁺CD25⁺ regulatory T cells. *J Exp Med* **201**, 1061–1067.
- [46] Hsieh CS, Lee HM, and Lio CW (2012). Selection of regulatory T cells in the thymus. *Nat Rev Immunol* **12**, 157–167.
- [47] Lu LF and Rudensky A (2009). Molecular orchestration of differentiation and function of regulatory T cells. *Genes Dev* **23**, 1270–1282.
- [48] Quezada SA, Peggs KS, Simpson TR, and Allison JP (2012). Shifting the equilibrium in cancer immunoediting: from tumor tolerance to eradication. *Immunol Rev* **241**, 104–118.

- [49] Koyama K, Kagamu H, Miura S, Hiura T, Miyabayashi T, Itoh R, Kuriyama H, Tanaka H, Tanaka J, Yoshizawa H, et al. (2008). Reciprocal CD4⁺ T-cell balance of effector CD62L^{low} CD4⁺ and CD62L^{high} CD25⁺ CD4⁺ regulatory T cells in small cell lung cancer reflects disease stage. *Clin Cancer Res* **14**, 6770–6779.
- [50] Ju S, Qiu H, Zhou X, Zhu B, Lv X, Huang X, Li J, Zhang Y, Liu L, Ge Y, et al. (2009). CD13⁺CD4⁺CD25^{hi} regulatory T cells exhibit higher suppressive function and increase with tumor stage in non-small cell lung cancer patients. *Cell Cycle* **8**, 2578–2585.
- [51] Huang CT, Workman CJ, Flies D, Pan X, Marson AL, Zhou G, Hipkiss EL, Ravi S, Kowalski J, Levitsky HI, et al. (2004). Role of LAG-3 in regulatory T cells. *Immunity* **21**, 503–513.
- [52] Rudensky AY (2011). Regulatory T cells and Foxp3. *Immunol Rev* **241**, 260–268.
- [53] Lo Re S, Lecocq M, Uwambayinema F, Yakoub Y, Delos M, Demoulin JB, Lucas S, Sparwasser T, Renauld JC, Lison D, et al. (2011). Platelet-derived growth factor-producing CD4⁺ Foxp3⁺ regulatory T lymphocytes promote lung fibrosis. *Am J Respir Crit Care Med* **184**, 1270–1281.
- [54] Granville CA, Memmott RM, Balogh A, Mariotti J, Kawabata S, Han W, Lopiccio J, Foley J, Liewehr DJ, Steinberg SM, et al. (2009). A central role for Foxp3⁺ regulatory T cells in K-Ras-driven lung tumorigenesis. *PLoS One* **4**, e5061.

Table W1. Primers Used for Mutational Analysis of the Mouse *K-RAS*, *TP53*, and *STK11* Genes and for IL-6, IL-1 β , and GM-CSF mRNA Expression.

Genes	Sense 5'→3'	Antisense 5'→3'
<i>K-RAS exon 2</i>	tgtaaaggcctgctgaaatg	cgtagggtcatactcatccaca
<i>K-RAS exon 3</i>	tgtgtttctcccttcaggga	tgcaggcataacaattagcaa
<i>TP53 exon 5-6</i>	tagttcccaccttgacacc	gacgcacaaccaaaacaaa
<i>TP53 exon 7</i>	tgccgaacaggtggaatgc	cagaagctggggagaagaaca
<i>TP53 exon 8-9</i>	ggggccttagtttacacaca	tgcgagagacagagccaata
<i>STK11 exon 1</i>	aaggggacgaggacaaga	gaagagccagaagtaggag
<i>STK11 exon 2</i>	caggtgtcacaggcaaacag	agcactattctgtccaggag
<i>STK11 exon 3</i>	gagagcagatgggtgggt	acctgggtttcctgacaatg
<i>STK11 exon 4-5</i>	catggatgggtgagacac	cactaggggaaaaccacagc
<i>STK11 exon 8</i>	ctgtagccggagcactaagg	tcatgttagctggctggaga
<i>STK11 exon 9</i>	gcttgcccttggagctactg	cactgtgaacaccagggatg
<i>IL-6</i>	acaaagccagagtccttcag	tggatggcttggctccta
<i>IL-1β</i>	gctgaaagctctccactca	aggccacaggattttgtcg
<i>GM-CSF</i>	caaggggccttgacat	atgaatccgcatagggtgt

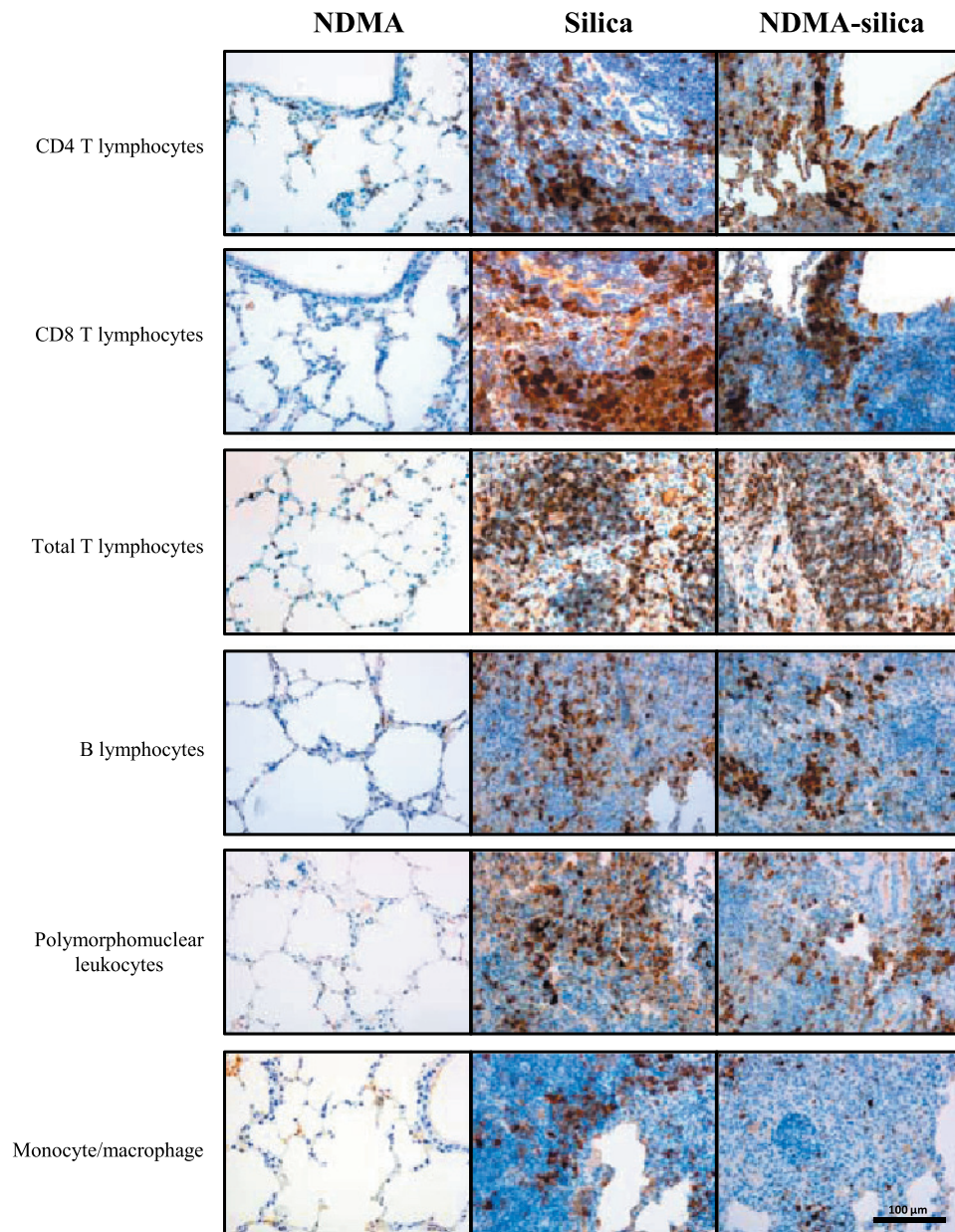


Figure W1. Illustrative examples of CD4 (CD4 T lymphocytes), CD8 (CD8 T lymphocytes), CD3 (total T lymphocytes), CD20 (B lymphocytes), myeloperoxidase (polymorphonuclear leukocytes), and CD68 (monocyte/macrophage) immunostainings in lungs from mice treated with NDMA-only, silica, and NDMA-silica.

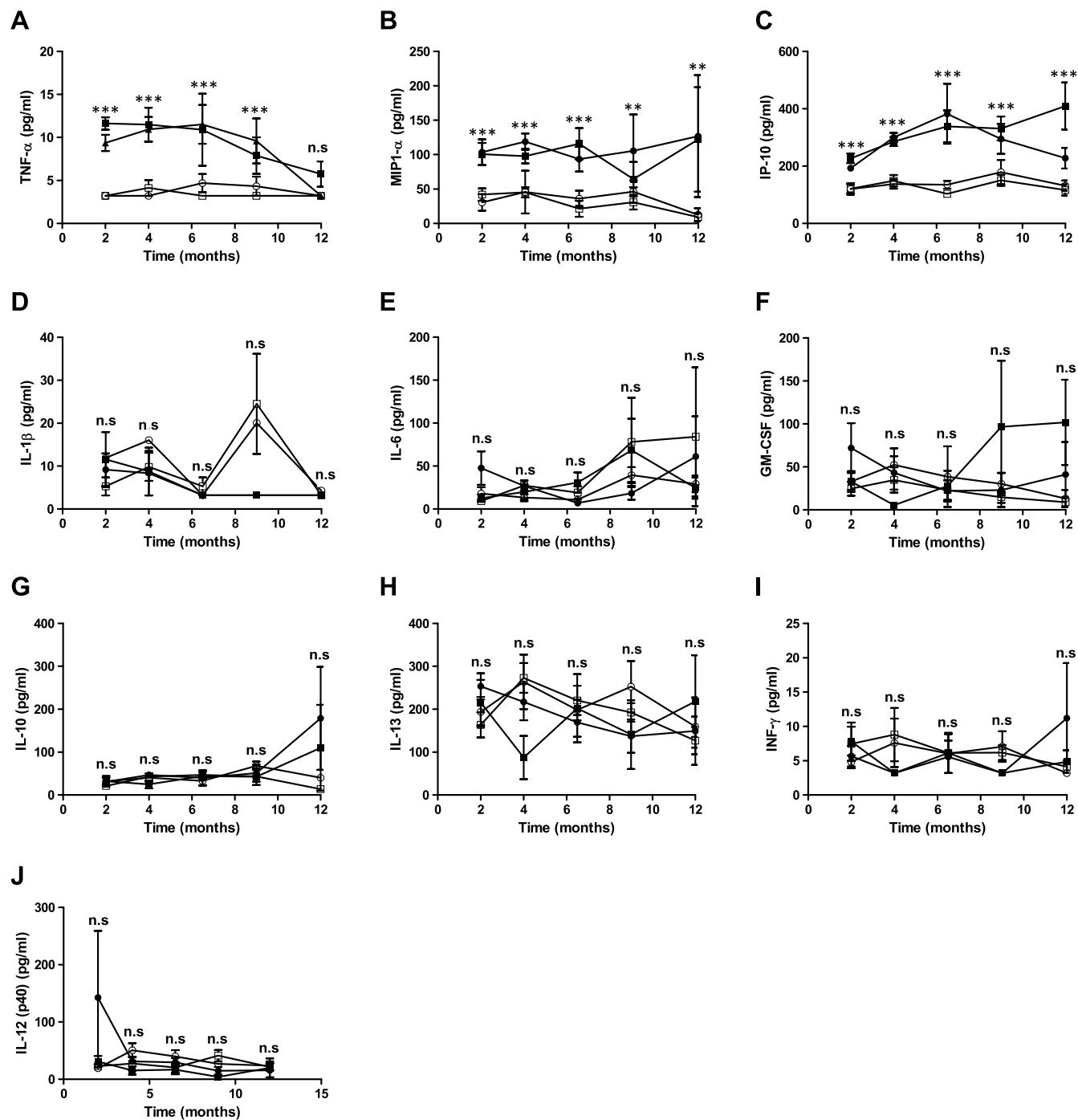


Figure W2. Plasma levels of (A) TNF- α , (B) MIP-1 α , (C) IP-10, (D) IL-1 β , (E) IL-6, (F) GM-CSF, (G) IL-10, (H) IL-13, (I) INF- γ , and (J) IL-12 (p40) in mice treated with saline (white circles), silica (black triangles), NDMA (white squares), and NDMA-silica (black squares) at different experimental points. Values represent the mean of plasma cytokine concentration from four mice \pm SEM. Differences between groups were analyzed at every experimental point using the Kruskal-Wallis test with post hoc Dunn comparison (n.s., $P > .05$; ** $P < .01$; *** $P < .001$).

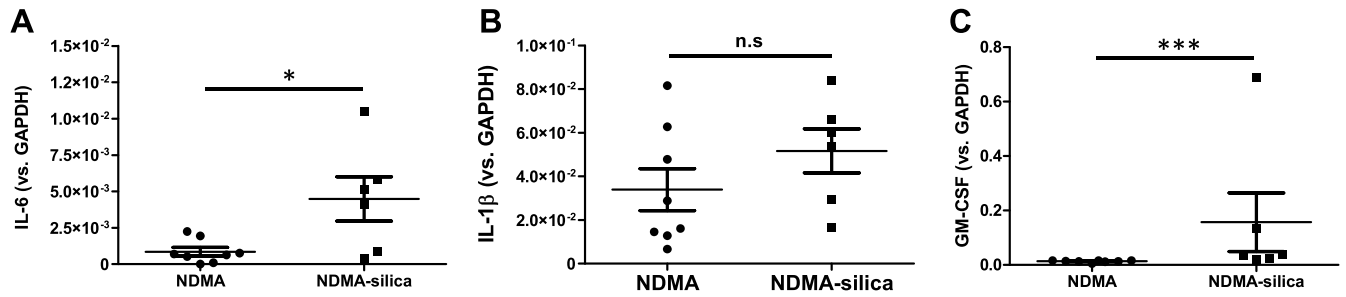


Figure W3. (A) IL-6, (B) IL-1 β , and (C) GM-CSF mRNA expression in lung lobes from mice treated with NDMA-only (eight lung lobes from eight mice) or NDMA-silica (six lung lobes from three mice) at month 12. The analysis was performed by real-time PCR using specific primers for all these genes (Table W1). *Glyceraldehyde 3-phosphate dehydrogenase (GAPDH)* was used as housekeeping gene. Differences between experimental groups were analyzed using the Mann-Whitney U test (n.s., $P > .05$; * $P < .05$; *** $P < .001$).

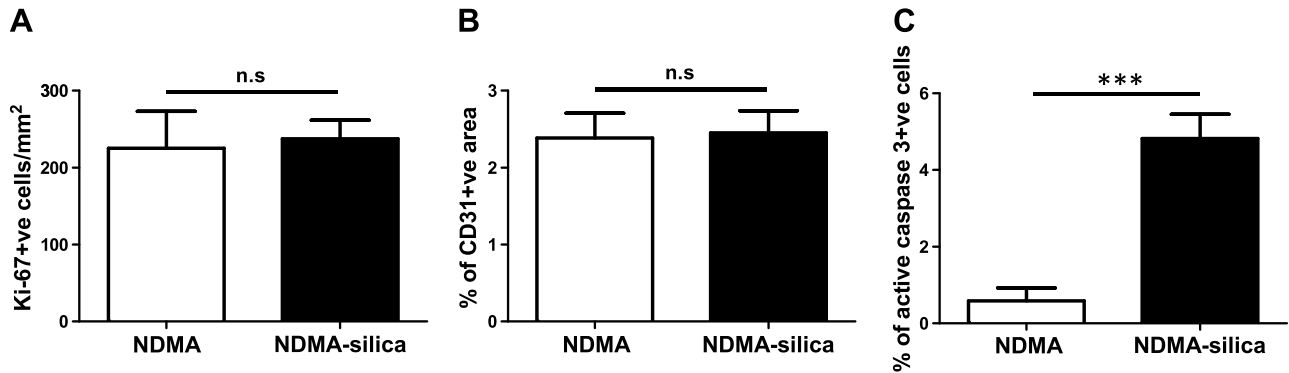


Figure W4. Quantitative analysis of proliferation, angiogenesis, and apoptosis of adenomas from NDMA- and NDMA-silica-treated mice. (A) Proliferation was measured as the number of positive immunostained Ki-67 cells per mm² of adenomas (NDMA, $n = 18$ lesions; NDMA-silica, $n = 63$ lesions). (B) Angiogenesis was quantified as the percentage of the area of adenoma positive for CD31 immunostaining (NDMA, $n = 28$ lesions; NDMA-silica, $n = 74$ lesions). (C) Apoptosis level was quantified as the percentage of positive active caspase-3-immunostained cells (NDMA, $n = 28$; NDMA-silica, $n = 74$). Values are represented as the means \pm SEM. Differences between groups were analyzed using a two-sided Mann-Whitney U test (ns, $P > .05$).

Table W2. Differentially Expressed Genes in Adenocarcinomas from NDMA-silica- and NDMA-Treated Mice* ($B \geq 0$; $|\log FC| \geq 1.5$).

Genes	Description	Log FC	P Value	B
Upregulated genes in NDMA-silica <i>versus</i> NDMA adenocarcinomas				
<i>Hunk</i>	Hormonally upregulated Neu-associated kinase	2.07	.0000051	3.68
<i>Dcpp1</i>	Demilune cell and parotid protein 1	1.67	.0000437	1.95
Downregulated genes in NDMA-silica <i>versus</i> NDMA adenocarcinomas				
<i>Maff</i>	V-maf musculoaponeurotic fibrosarcoma oncogene family, protein F (avian)	-1.54	.0003058	0.33
<i>Etv1</i>	Ets variant gene 1	-1.66	.0001147	1.15
<i>Gm1965</i>	Gene model 1965, (NCBI)	-1.72	.0000123	2.98
<i>Carm1</i>	Coactivator-associated arginine methyltransferase 1	-1.79	.0002850	0.39
<i>Plk2</i>	Polo-like kinase 2 (Drosophila)	-1.87	.0003810	0.15
<i>Tcirg1</i>	T-cell, immune regulator 1, ATPase, H ⁺ transporting, lysosomal V0 protein A3	-2.06	.0000497	1.84
<i>Kdelc1</i>	KDEL (Lys-Asp-Glu-Leu) containing 1	-2.07	.0001641	0.85
<i>Aanat</i>	Arylalkylamine <i>N</i> -acetyltransferase	-2.22	.0000979	1.28
<i>Muc4</i>	Mucin 4	-2.65	.0000000	8.69
<i>Tcf25</i>	Transcription factor 25 (basic helix-loop-helix)	-3.09	.0000019	4.45
<i>Rbm12</i>	RNA binding motif protein 12	-3.17	.0000019	4.47
<i>Serpina3c</i>	Serine (or cysteine) peptidase inhibitor, clade A, member 3C	-3.31	.0000060	3.55

*For each candidate *P* value, *B* statistic and log FC are shown.

Table W3. List of GO Categories Enriched in the Differentially Expressed Genes of NDMA-Silica Tumors when Compared to the NDMA Tumors.

	Term	P Value	Genes
GO enriched in adenomas NDMA-silica <i>versus</i> NDMA	Response to external stimulus	.000084	<i>Serpina1c</i> , <i>Saa3</i> , <i>C1qc</i> , <i>Hsd12</i> , <i>S100a8</i> , <i>Serpina3n</i> , <i>Lta</i> , <i>Etv1</i> , <i>S100a9</i>
	Acute inflammatory response	.000095	<i>Serpina1c</i> , <i>Saa3</i> , <i>C1qc</i> , <i>Hsd12</i> , <i>Serpina3n</i>
	Inflammatory response	.00051	<i>Serpina1c</i> , <i>Saa3</i> , <i>C1qc</i> , <i>Hsd12</i> , <i>Serpina3n</i> , <i>Lta</i>
	Immune system process	.00074	<i>Nfkb1a</i> , <i>Lax1</i> , <i>C1qc</i> , <i>Hsd12</i> , <i>H2-Q6</i> , <i>Lta</i> , <i>Mitf</i> , <i>S100a9</i> , <i>Bank1</i>
	Acute-phase response	.0028	<i>Serpina1c</i> , <i>Saa3</i> , <i>Serpina3n</i>
	Protease inhibitor activity	.015	<i>Serpina1c</i> , <i>Stfa3</i> , <i>Stfa3</i> , <i>Serpina3n</i> , <i>Serpina3c</i>
	Enzyme binding	.026	<i>Nfkb1a</i> , <i>Lax1</i> , <i>Pstpip1</i> , <i>Bank1</i>
	Positive regulation of biologic process	.028	<i>Lax1</i> , <i>C1qc</i> , <i>Col15a1</i> , <i>Lta</i> , <i>Etv1</i> , <i>Mitf</i> , <i>Tcf7l2</i> , <i>Mef2c</i>
	Receptor binding	.04	<i>C1qc</i> , <i>Lta</i> , <i>Gast</i> , <i>Retnla</i> , <i>Retnlg</i> , <i>Bank1</i>
	Regulation of cellular process	.0074	<i>Cycs</i> , <i>Ston1</i> , <i>Tcf25</i> , <i>Rabgap1l</i> , <i>Plk2</i> , <i>Maff</i> , <i>Ascl3</i> , <i>Irf6</i> , <i>Etv1</i> , <i>Carm1</i> , <i>Cnot6l</i> , <i>Phf10</i>
GO enriched in adenocarcinomas NDMA-silica <i>versus</i> NDMA	Biologic regulation	.010	<i>Cycs</i> , <i>Tcf25</i> , <i>Rabgap1l</i> , <i>Ascl3</i> , <i>Maff</i> , <i>Irf6</i> , <i>Cnot6l</i> , <i>Phf10</i> , <i>Ston1</i> , <i>Plk2</i> , <i>Carm1</i> , <i>Etv1</i> , <i>Npr1</i>
	Nucleobase, nucleoside, nucleotide, and nucleic acid metabolic process	.012	<i>Msh5</i> , <i>Tcf25</i> , <i>Cstf1</i> , <i>Maff</i> , <i>Ascl3</i> , <i>Irf6</i> , <i>Etv1</i> , <i>Carm1</i> , <i>Cnot6l</i> , <i>Npr1</i> , <i>Phf10</i>
	Nucleic acid binding	.016	<i>Msh5</i> , <i>Tcf25</i> , <i>Cstf1</i> , <i>Rbm12</i> , <i>Maff</i> , <i>Ascl3</i> , <i>Irf6</i> , <i>Etv1</i> , <i>Cnot6l</i> , <i>Phf10</i>
	Transcription regulator activity	.021	<i>Tcf25</i> , <i>Maff</i> , <i>Ascl3</i> , <i>Irf6</i> , <i>Etv1</i> , <i>Carm1</i>
	RNA metabolic process	.023	<i>Tcf25</i> , <i>Cstf1</i> , <i>Maff</i> , <i>Ascl3</i> , <i>Irf6</i> , <i>Etv1</i> , <i>Carm1</i> , <i>Cnot6l</i> , <i>Phf10</i>
	Regulation of transcription, DNA-dependent	.026	<i>Tcf25</i> , <i>Maff</i> , <i>Ascl3</i> , <i>Irf6</i> , <i>Etv1</i> , <i>Carm1</i> , <i>Cnot6l</i> , <i>Phf10</i>
	Metabolic process	.029	<i>Cycs</i> , <i>Tcf25</i> , <i>Aanat</i> , <i>Ascl3</i> , <i>Maff</i> , <i>Irf6</i> , <i>Cnot6l</i> , <i>Phf10</i> , <i>Msh5</i> , <i>Hunk</i> , <i>Cstf1</i> , <i>Plk2</i> , <i>Mthfd1l</i> , <i>Etv1</i> , <i>Carm1</i> , <i>Npr1</i>

P value is shown for each GO category.